

# Observed equatorward propagation and chimney effect of near-inertial waves in the mid-latitude ocean

Xiaolong Yu<sup>1,2,3</sup>, Alberto C. Naveira Garabato<sup>4</sup>, Clément Vic<sup>5</sup>, Jonathan Gula<sup>5,6</sup>, Anna C. Savage<sup>7</sup>, Jinbo Wang<sup>8</sup>, Amy F. Waterhouse<sup>7</sup>, Jennifer A. MacKinnon<sup>7</sup>

<sup>1</sup>School of Marine Sciences, Sun Yat-sen University, Zhuhai, China

<sup>2</sup>Southern Marine Science and Engineering Guangdong Laboratory (Zhuhai), Zhuhai, China

<sup>3</sup>Guangdong Provincial Key Laboratory of Marine Resources and Coastal Engineering, Guangzhou, China

<sup>4</sup>Ocean and Earth Science, University of Southampton, Southampton, UK

<sup>5</sup>Univ Brest, CNRS, IRD, Ifremer, Laboratoire d'Océanographie Physique et Spatiale (LOPS), IUEM,

Brest, France

<sup>6</sup>Institut Universitaire de France (IUF), Paris, France

<sup>7</sup>Scripps Institution of Oceanography, University of California, San Diego, La Jolla, California, USA

<sup>8</sup>Jet Propulsion Laboratory, California Institute of Technology, Pasadena, California, USA

## Key Points:

- We provide observational evidence of downward- and equatorward-propagating near-inertial waves over a full annual cycle.
- Enhanced near-inertial kinetic energy and vertical shear are found preferentially in regions of anticyclonic vorticity.
- The chimney effect for near-inertial waves is very likely controlled by mesoscale, rather than submesoscale, anticyclones.

**Abstract**

The propagation characteristics of near-inertial waves (NIWs) and how mesoscale and submesoscale processes affect the waves' vertical penetration are investigated using observations from a mooring array located in the northeast Atlantic. The year-long observations show that near-inertial motions are mainly generated by local wind forcing, and that they radiate equatorward and downward following several strong wind events (wind stress  $\gtrsim 0.5 \text{ N m}^{-2}$ ). Observational estimates of horizontal group speed typically exceed those of vertical group speed by two orders of magnitude, consistent with predictions from the dispersion relation. Enhanced near-inertial kinetic energy and vertical shear are found only in mesoscale anticyclones with Rossby number of  $O(0.1)$ . By contrast, submesoscale motions with order one Rossby number have little effect on the trapping and vertical penetration of NIWs, due to their smaller horizontal scales, shorter time scales and confined vertical extent compared to mesoscale eddies.

**Plain Language Summary**

Near-inertial waves (NIWs) are excited mainly by variable winds at the ocean surface and can carry their energy into the ocean interior, thus playing an important role in mixing the deep ocean. However, the propagation behaviors of NIWs, and how such waves are affected by mesoscale and submesoscale processes, are still understudied, especially over periods of months to years. In this study, we examine an annual cycle of wind-generated NIWs based on moored observations in a typical open-ocean region of the northeast Atlantic. Our results show that NIWs propagate downward and equatorward following several strong wind events. Enhanced near-inertial kinetic energy and vertical shear are found preferentially in regions of anticyclonic vorticity with Rossby number of  $O(0.1)$ . By contrast, submesoscale anticyclones with Rossby number of  $O(1)$  are ineffective at trapping and accelerating near-inertial motions into the ocean interior. This is due to the smaller horizontal scales, shorter time scales and confined vertical extent of submesoscale motions compared to mesoscale eddies. Our findings highlight the major role of mesoscale anticyclones in draining NIWs from the upper ocean to the ocean interior, and have implications for detecting regions of active turbulent mixing driven by NIWs in the deep ocean.

## 51 1 Introduction

52 Near-inertial waves (NIWs), primarily generated by strong resonant winds blowing on  
 53 the sea surface, are a crucial contributor to ocean mixing (Alford et al., 2016; Thomas &  
 54 Zhai, 2022). NIWs are oscillatory, unbalanced internal wave motions with frequencies close  
 55 to the local inertial frequency, and account for a major portion of internal wave energy and  
 56 shear (Garrett, 2001). Wind generation of near-inertial motions can be generally considered  
 57 as a two-stage process, featuring an initial stage with resonant wind work on the ocean sur-  
 58 face currents that generates surface mixed-layer near-inertial oscillations, and a subsequent  
 59 stage with propagation and decay of those motions in the form of NIWs. Global estimates  
 60 of the wind energy flux into NIWs are in the range of 0.3-1.5 TW (Jiang et al., 2005; Rimac  
 61 et al., 2013), which is comparable to the global energy conversion rate from external to  
 62 internal tides in the deep ocean (about 1 TW; Egbert & Ray, 2000). Aside of 15-25% of  
 63 the energy input by the wind work radiating away from their generation regions in the form  
 64 of low-mode NIWs (Alford, 2003; Alford & Zhao, 2007; Simmons & Alford, 2012), over  
 65 half of near-inertial energy is thought to locally dissipate in the upper few hundred meters  
 66 of the ocean (Zhai et al., 2009; Alford, 2020). Nevertheless, the rest of the wave energy  
 67 has been suggested to radiate downward (e.g., Leaman & Sanford, 1975; Gill, 1984) and to  
 68 penetrate to large depths (e.g., 3000 m; Silverthorne & Toole, 2009). Hence, the substan-  
 69 tial downward-propagating NIWs are an important source of energy for driving deep-ocean  
 70 mixing and maintaining abyssal stratification (Ferrari & Wunsch, 2009; Whalen et al., 2020;  
 71 Qu et al., 2021).

72 A key factor that affects the vertical penetration of NIWs is the background vorticity.  
 73 The principal effect of vorticity is to shift the lower bound of the internal wave band from  
 74 the local inertial frequency  $f$  to the effective inertial frequency,  $f_{eff} = f + \zeta/2$ , where  $\zeta$  is  
 75 the vertical component of the relative vorticity (Kunze, 1985). Consequently, NIWs can be  
 76 trapped in regions of anticyclonic vorticity where  $f_{eff}$  is lower than  $f$ . Lee and Niiler (1998)  
 77 firstly termed ‘the inertial chimney effect’ the trapping and accumulation of near-inertial  
 78 energy in regions of anticyclonic vorticity. This effect has been explored by, for example,  
 79 Zhai et al. (2005, 2007), who analyzed mesoscale-permitting numerical simulations to show  
 80 that anticyclonic eddies act to drain near-inertial energy from the surface to the deep ocean.  
 81 More recently, the inertial chimney effect of turbulent baroclinic quasi-geostrophic eddies  
 82 was also demonstrated by Asselin and Young (2020) under an idealized storm scenario, where  
 83 they referred to this effect as ‘inertial drainpipe’. Vic et al. (2021) examined the association  
 84 of mooring-measured near-inertial energy with altimetry-derived relative vorticity with a  
 85 horizontal resolution of  $O(100 \text{ km})$  over the Mid-Atlantic Ridge, and showed that near-  
 86 inertial energy is preferentially funneled down within anticyclonic flows. To our knowledge,  
 87 observational assessment of the chimney effect down to the submesoscales ( $0.1\text{-}10 \text{ km}$ ) has  
 88 not yet been performed.

89 Compared to the vertical propagation of NIWs, their meridional propagation, however,  
 90 remains elusive. The theory of  $\beta$ -refraction predicts an equatorward propagation of NIWs  
 91 due to the latitudinal variation in the inertial frequency (Garrett, 2001). This proposition  
 92 is endorsed by near-inertial energy flux estimates from mooring observations in the open  
 93 ocean (e.g., Alford, 2003) and on the continental shelf (e.g., Schlosser et al., 2019). Such  
 94 calculations typically require a flat-bottomed ocean and full-depth measurements, and thus  
 95 existing observations are sparse. By contrast, numerical and observational studies have also  
 96 shown that NIWs can propagate poleward. Based on turning-point theory and a numerical  
 97 model, Fu (1981) suggested that the observed local inertial peak over smooth topography  
 98 could be interpreted in terms of poleward-propagating waves generated at lower latitudes.  
 99 The poleward propagation of NIWs can also be caused by the background flow (e.g., Tort &  
 100 Winters, 2018; Jeon et al., 2019; Huang et al., 2021). Tort and Winters (2018) demonstrated  
 101 a scale selection mechanism by which the super-inertial component of NIWs is able to prop-  
 102 agate poleward over long distances in the presence of mesoscale turbulence with horizontal  
 103 scales considerably smaller than the width of the storm track.

104 In this study, we focus on the propagation of NIWs in a typical mid-ocean region using  
 105 nine year-long mooring records that resolve the spatio-temporal scales of the submesoscales.  
 106 We show that wind-generated NIWs propagate equatorward and downward in the study  
 107 region. The waves' vertical and meridional group speeds are directly quantified from ob-  
 108 servations, and are found to be consistent with the properties determined by the dispersion  
 109 relation. The inertial chimney effect is observed below the mixed layer. However, enhanced  
 110 near-inertial kinetic energy and vertical shear are only found in mesoscale anticyclones of  
 111 Rossby number  $O(0.1)$  rather than in submesoscale anticyclones of Rossby number  $O(1)$ .

## 112 2 Observations and Methods

### 113 2.1 Mooring observations

114 Nine bottom-anchored subsurface moorings were deployed over the Porcupine Abyssal  
 115 Plain ( $48.63\text{--}48.75^\circ\text{N}$ ,  $16.09\text{--}16.27^\circ\text{W}$ ) site in the northeast Atlantic Ocean for the period  
 116 September 2012 - September 2013 (Figure 1a), as part of the OSMOSIS (Ocean Surface  
 117 Mixing, Ocean Submesoscale Interaction Study) experiment (Buckingham et al., 2016, 2019;  
 118 Yu et al., 2019, 2021; Naveira Garabato et al., 2022). The mooring site is over a smooth  
 119 abyssal plain of depth close to 4800 m. This region is expected to be representative of the  
 120 mid-latitude open ocean far away from western boundaries and complex topography. The  
 121 nine moorings were arranged in two concentric quadrilaterals with side lengths of  $\sim 13$  km  
 122 (outer cluster) and  $\sim 2$  km (inner cluster) around a centrally located single mooring (Figure  
 123 1b). Mooring sensors comprised a series of paired Nortek Aquadopp acoustic current meters  
 124 (ACMs) and Seabird MicroCAT conductivity-temperature-depth (CTD) sensors at different  
 125 depths, spanning the approximate depth interval 30-530 m. The central mooring was the  
 126 most heavily instrumented, with 13 CTD/ACM pairs. The inner and outer moorings had  
 127 seven and five such pairs, respectively. The central and four inner moorings were also  
 128 instrumented with 75-KHz unit upward-looking Acoustic Doppler Current Profilers (ADCP)  
 129 at about 450 m, which measured horizontal velocity in 8-m bins and formed ensembles every  
 130 60 minutes. In addition, the mooring measurements were complemented by hydrographic  
 131 observations acquired by two ocean gliders that navigated in a bow-tie pattern across the  
 132 mooring array for the entire sampling period (Damerell et al., 2016; Thompson et al., 2016).  
 133 The mixed layer depth,  $H_{ML}$ , is calculated from coincident glider data using a threshold  
 134 value of potential density increase ( $\Delta\rho = 0.03 \text{ kg m}^{-3}$ ) from a near-surface value at 10 m  
 135 (Damerell et al., 2016).

136 Mooring measurements captured the mixed layer during winter and early spring months,  
 137 and the pycnocline plus part of the ocean interior throughout the year. Horizontal veloc-  
 138 ity, temperature, salinity and pressure observations were obtained by ACMs and CTDs,  
 139 with sampling intervals of 10 and 5 minutes, respectively. For each mooring, we linearly  
 140 interpolated measurements of horizontal velocity, temperature and salinity onto surfaces of  
 141 constant depth at 10-m intervals between depths of 50 m and 520 m, and onto uniform  
 142 10-minute intervals between 5 September 2012 and 5 September 2013. Subsequently, the  
 143 10-minute horizontal velocities were averaged onto hourly intervals.

### 144 2.2 Wind data

145 The buoy of the OSMOSIS moorings contained meteorological sensors. Unfortunately,  
 146 the buoy sank shortly after deployment. Wind data are instead taken from the ECMWF  
 147 (European Centre for Medium-Range Weather Forecasting) ERA-Interim reanalysis surface  
 148 wind fields (Dee et al., 2011). Zonal and meridional reanalysis winds are obtained at the  
 149 grid point closest to the central mooring site with a time interval of 3 hours for the record  
 150 year. Wind measurements from the K1 buoy, 250 km away from the OSMOSIS mooring site  
 151 (Figure 1a), are used to validate the reanalysis wind fields. The K1 buoy sampled at hourly  
 152 intervals from 5 September to 28 December 2012. Wind speed was converted to stress using

153 a speed-dependent drag coefficient (Large & Pond, 1981). The reanalysis winds show a good  
 154 agreement with the measured winds, with a correlation coefficient of 0.74 (Figure 1c).

### 155 2.3 Band pass filtering

156 Moored horizontal velocities are bandpass filtered around the near-inertial frequency,  
 157 where the near-inertial band (denoted by the subscript ‘*NI*’) is defined as  $\{0.9, 1.1\}f$ ,  
 158 with  $f = 2\Omega \sin \phi$  as the inertial frequency,  $\Omega$  as the Earth’s angular velocity and  $\phi$  as  
 159 latitude. The inertial period is approximately 16 hr at the OSMOSIS site. The rotary  
 160 frequency spectra of horizontal velocity show a prominent peak rising within the near-  
 161 inertial band for clockwise motions but not for counter-clockwise motions, consistent with  
 162 the expectation that near-inertial flows are strongly clockwise-polarized (Figure S1 in the  
 163 supporting information). We did not find a significant sensitivity of our results (section 3)  
 164 to the bandwidth of the near-inertial band. Near-inertial velocity is isolated by means of a  
 165 fourth-order Butterworth filter applied in the time domain. Following bandpassing, near-  
 166 inertial kinetic energy and vertical shear are respectively quantified as  $KE_{NI} = \frac{1}{2}\rho_0|\mathbf{u}_{NI}|^2$   
 167 and  $S_{NI} = |\partial \mathbf{u}_{NI}/\partial z|^2$ , where  $\mathbf{u} = (u, v)$  is the horizontal velocity,  $\rho_0 = 1025 \text{ kg m}^{-3}$  is a  
 168 reference density and  $z$  is the vertical coordinate. As previous OSMOSIS studies have shown  
 169 that the region underwent a seasonal cycle in the vertical stratification (e.g., Buckingham  
 170 et al., 2016; Erickson et al., 2020), monthly moving averaged buoyancy frequency is used to  
 171 obtain ‘Wentzel-Kramers-Brillouin (WKB)’ scaled near-inertial kinetic energy  $KE_{NI}^{WKB}$  and  
 172 vertical shear  $S_{NI}^{WKB}$ . To account for vertical wavenumber changes, a WKB-stretched depth  
 173 is applied (see the supporting information for methodology). Further, the near-inertial wind  
 174 work is defined as  $\Pi_{NI} = \boldsymbol{\tau}_{NI} \cdot \mathbf{u}_{NI}$ , where  $\boldsymbol{\tau}$  is the surface wind stress vector and  $\mathbf{u}_{NI}$  the  
 175 mixed-layer near-inertial currents obtained from the shallowest available ACMs record in  
 176 the central mooring ( $\sim 50 \text{ m}$ , 57.1% of the time during the year within the mixed layer).

## 177 3 Results

### 178 3.1 Annual cycle of wind-generated near-inertial waves

179 Near-inertial wind work is highly variable throughout the entire year, with the wind  
 180 energy flux into near-inertial motions dominated by several intermittent events with duration  
 181 of several days (Figure 1d). The cumulative near-inertial wind work with time shows a  
 182 distinct ‘staircase’ structure during the periods of strong resonant forcing (Figure 1e), which  
 183 coincides well with the elevated  $KE_{NI}^{WKB}$  in the upper ocean (e.g., late December and mid-  
 184 January; Figure 1f). These results suggest that the observed near-inertial energy is likely  
 185 locally generated by surface wind forcing. This is further supported by the agreement  
 186 between the near-inertial wind work estimated from observed velocity and reanalysis winds  
 187 and that from the slab model solely forced by the reanalysis winds (see the supporting  
 188 information for methodology). The typical amplitude of  $KE_{NI}^{WKB}$  during near-inertial wave  
 189 events is of order  $10 \text{ J m}^{-3}$ , corresponding to a horizontal velocity scale of  $\sim 0.1 \text{ m s}^{-1}$ . This  
 190 value is comparable in magnitude with the global average near-inertial velocity (Park et  
 191 al., 2005; Chaigneau et al., 2008). Further, most of the increase in cumulative near-inertial  
 192 wind work is seen in winter (December-March; Figure 1e), implying a seasonal cycle of  
 193 wind-generated NIWs. The vertical profiles of  $KE_{NI}^{WKB}$  in winter and summer also denote  
 194 seasonality of near-inertial energy, with the magnitude being much higher in winter at all  
 195 measured depths (Figure S2).

196 Plueddemann and Farrar (2006) found that the slab model might overestimate the  
 197 near-inertial wind work, and Alford (2020) further indicated that this overestimation likely  
 198 occurs when the mixed layer depth  $H_{ML}$  is shallow compared to the scaling  $H^* = u^*/\sqrt{N^* f}$ ,  
 199 where  $u^* = \sqrt{\tau/\rho_{air}}$  is the friction velocity of the imposed stress,  $\rho_{air}$  the density of air and  
 200  $N^*$  the buoyancy frequency just below the mixed layer. In the  $H_{ML} \lesssim H^*$  case, the slab  
 201 model may not account for the mixing and momentum injected by the winds. We examined  
 202 this possibility in our data and found that the glider-derived mixed layer depth is largely

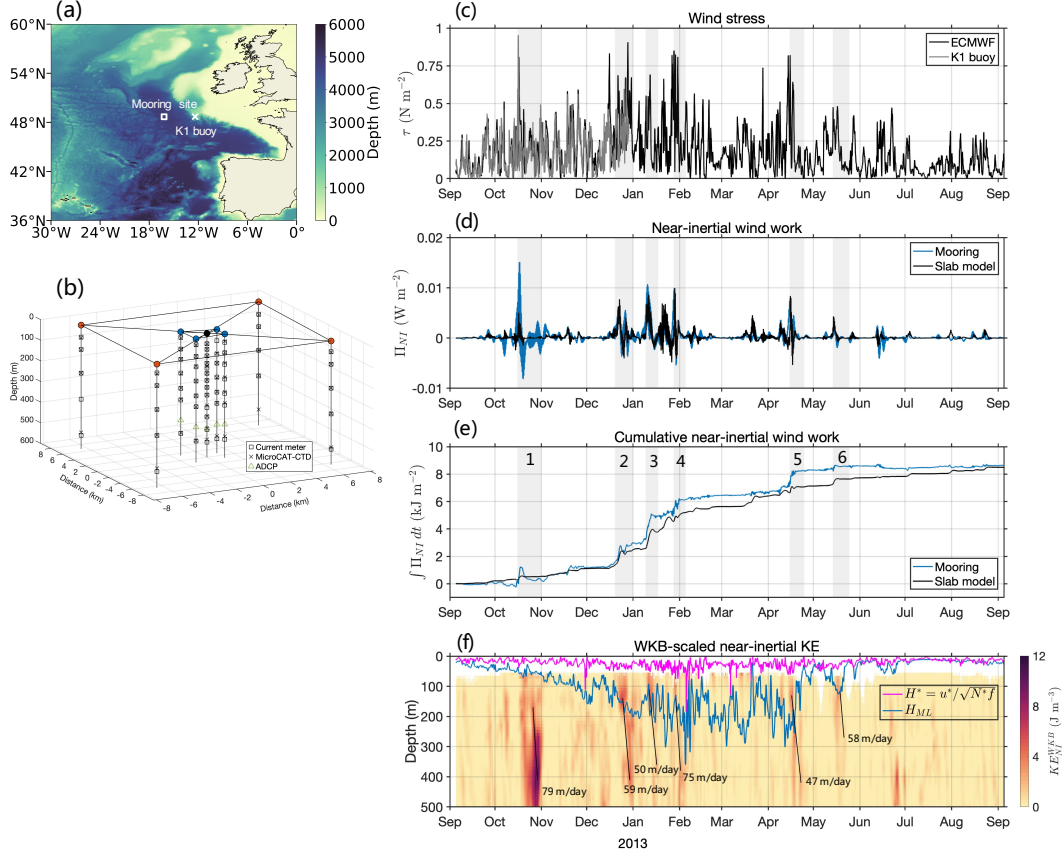


**Figure 1.** (a) OSMOSIS study region in the Northeast Atlantic, with bathymetry shown in the colormap on the right. The white rectangle and white cross denote the locations of the OSMOSIS mooring array and the K1 buoy, respectively. (b) 3-d configuration of the OSMOSIS array (central mooring marked by black circle, inner moorings by blue circles, and outer moorings by red circles), with positions of current meters, CTDs and ADCPs respectively marked by black squares, black crosses and green triangles. (c) Time series of wind stress estimated from the ECMWF reanalysis winds (black) and the K1 buoy measurements (gray). (d) Time series of near-inertial wind work computed from the ECMWF reanalysis winds and observed mixed-layer near-inertial currents (blue), and from the slab model driven by the ECMWF reanalysis winds (black). (e) Time integral of (d) showing the cumulative wind energy input to the mixed layer from each flux estimate for the central mooring deployment period. (f) Time series of WKB-scaled near-inertial kinetic energy observed by the current meters at the central mooring. The blue and pink lines respectively indicate the glider-based mixed layer depth  $H_{ML}$  and the  $H^*$  scaling (section 3.1). Periods of the six near-inertial events are shaded gray in (c-e) and are labeled in (e). The duration of each event is mainly chosen to include near-inertial energy peaks from all moorings. The estimated downward group velocity of each event is indicated in (f).

203 deeper than  $H^*$  throughout the year, with the only exception in summer when  $KE_{NI}^{WKB}$  is  
 204 weak (June-August).

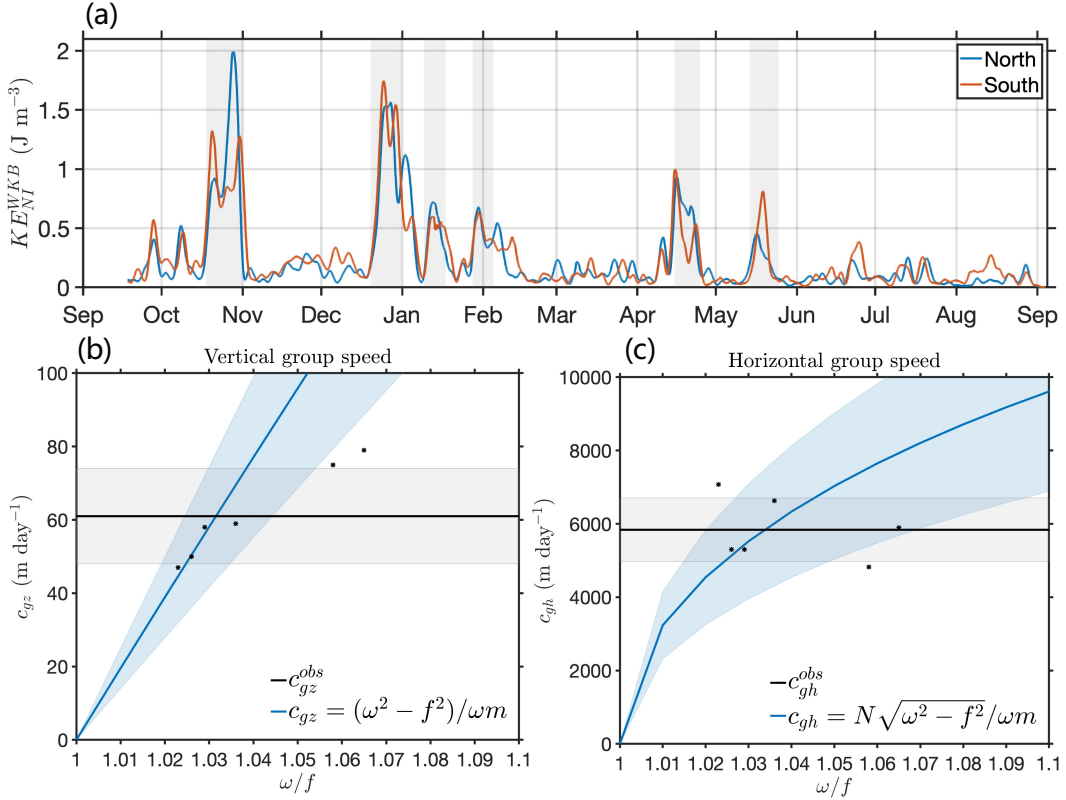


**Figure 2.** (a) Time series of WKB-scaled near-inertial kinetic energy estimated from outer moorings in the north (blue) and south (orange). Both estimates are low-pass filtered over 14.5 hr (corresponding to a frequency of  $1.1f$ ) to remove tidal and higher-frequency signals, and are then depth-averaged over all observed depths (50–520 m). (b) Comparison of six event-averaged vertical group speed estimates from observations (black) and from the dispersion curve for  $m = 2\pi/652 \text{ m}$  (blue). The shading represents one standard deviation. (c) Same as (b) but for horizontal group speed. Scattered dots in (b-c) represent estimates of the six near-inertial wave events.

205

### 3.2 Downward and equatorward propagation of near-inertial waves

206

Six major near-inertial wave events are identified throughout the year (see Figure 1e),  
 207 based on large wind stress ( $\gtrsim 0.5 \text{ N m}^{-2}$ ), net near-inertial wind energy input and enhanced  
 208 near-inertial kinetic energy. In the vertical, a dominance of downward propagation is con-  
 209 firmed by the rotary vertical wavenumber spectra of  $KE_{NI}^{WKB}$  and  $S_{NI}^{WKB}$  (Figure S3),  
 210 evidenced by the dominant clockwise rotation of horizontal velocity and shear vectors with  
 211 depth (Leaman & Sanford, 1975). Then, the vertical group speed can be estimated by  
 212 identifying near-inertial wave packets and the associated downward progression of kinetic  
 213 energy maxima over time (Figure 1f). We obtain a mean vertical group speed  $c_{gz}^{obs}$  with one  
 214 standard deviation of  $61 \pm 13 \text{ m day}^{-1}$  for the six identified near-inertial events. Following  
 215 Vic et al. (2021), we use mooring-based vertical group speed and vertical phase speed to  
 216 constrain the vertical wavenumber  $m$ . For waves with frequencies close to  $f$ , the equation  
 217 for  $m$  is  $(c_{\phi z}^{obs})^2 m^2 - c_{gz}^{obs} f m - f^2 = 0$ , where  $c_{\phi z}^{obs}$  is the vertical phase speed computed by

218 connecting constant-phase velocity points as a function of depth. For the six near-inertial  
 219 wave events, the mean vertical wavelength,  $2\pi/m$ , is quantified as  $652\pm185$  m.

220 The spatial arrangement of the mooring array also allows us to explore the meridional  
 221 propagation of NIWs. Comparison of the time series of  $KE_{NI}^{WKB}$  obtained from various  
 222 moorings shows that the near-inertial kinetic energy peaks in the south almost always lag  
 223 behind those in the north, suggesting that NIWs may propagate predominantly from north  
 224 to south (i.e., equatorward in the Northern Hemisphere; Figure 2a). This indication of  
 225 equatorward propagation is further confirmed by two lines of evidence. First, near-inertial  
 226 kinetic energy within the mooring array is highly coherent, with the magnitude-squared  
 227 coherence of near-inertial velocities  $\sim 0.8$  between inner moorings and  $\sim 0.6$  between outer  
 228 moorings, consistent with all moorings having captured the same near-inertial wave events.  
 229 Second, unlagged near-inertial kinetic energy peaks are commonly observed a few inertial  
 230 periods before the lagged peaks (e.g., events 1,2,4,5), with the former stemming from circular  
 231 inertial oscillations in the mixed layer and the latter from propagating NIWs below the mixed  
 232 layer. Then, we quantify the meridional group velocity using their meridional distance and  
 233 respective travel time. The travel time is identified as the temporal lag for which the lagged  
 234 correlation of depth-averaged near-inertial kinetic energy in the northern and southern outer  
 235 moorings is maximum. This gives a mean meridional group speed  $c_{gh}^{obs}$  of  $5875\pm864$  m day $^{-1}$ .

236 The frequency and horizontal scale of NIWs can be diagnosed by linking the observed  
 237 group speed estimates to the dispersion relation of NIWs (see the supporting information  
 238 for methodology), which is written as  $(\omega^2 - f^2)m^2 = N^2k_h^2$ , where  $\omega$  is the frequency and  
 239  $k_h$  the horizontal wavenumber. The observed  $c_{gz}^{obs}$  and  $c_{gh}^{obs}$  are broadly consistent with the  
 240 resulting dispersion curves in Figures 2b-c. Based on these wave properties, we can obtain  
 241 the mean frequency  $\omega = 1.039\pm0.018f$  and the horizontal wavelength  $2\pi/k_h = 79\pm28$  km  
 242 from the dispersion relation. The latter is consistent with the frequency structure function  
 243 diagnostics of Callies et al. (2020), who concluded that near-inertial motions have horizontal  
 244 wavelengths larger than the largest scale sampled by the outer mooring array. Detailed  
 245 properties of the six near-inertial events are given in Table S1.

### 246 3.3 Chimney effect

247 To assess the inertial chimney effect at different spatial scales, the vertical component  
 248 of the relative vorticity,  $\zeta = \frac{\partial v}{\partial x} - \frac{\partial u}{\partial y}$ , is respectively estimated from velocity gradients from  
 249 the inner and outer mooring clusters. The chimney effect for near-inertial kinetic energy  
 250 and vertical shear is illustrated by Figure 3, which displays the two-dimensional probability  
 251 density functions of Rossby number,  $\zeta/f$ , against  $KE_{NI}^{WKB}$  and  $S_{NI}^{WKB}$  and their associated  
 252 vertical structures. All terms are computed at the central mooring site, and include all  
 253 observed depths (50–520 m). For both spatial scales, near-inertial kinetic energy (Figures  
 254 3a-b) and vertical shear (Figures 3d-e) are found to be significantly intensified in regions  
 255 of anticyclonic vorticity (i.e.,  $\zeta/f < 0$ ). Such intensification in anticyclonic regimes is  
 256 more apparent for near-inertial kinetic energy, which is typically contained mostly in the  
 257 first few vertical modes (e.g., Raja et al., 2022), compared to near-inertial vertical shear,  
 258 which is contained mostly in higher vertical modes (e.g., Alford et al., 2017). Note that  
 259 horizontal scales of  $O(1$  km) and  $O(10$  km) are expected to be resolved by the inner and  
 260 outer mooring clusters, respectively. The inner mooring-based Rossby number  $\zeta_{Inner}/f$   
 261 reflects the signature of submesoscale flows with a positive skewness (Buckingham et al.,  
 262 2016) and a range from  $-0.8$  to  $1.2$ , which is 2–3 times larger than the outer mooring-based  
 263 Rossby number  $\zeta_{Outer}/f$  of  $-0.4$  to  $0.4$  (cf. Figures 3a and b). However, the enhanced  
 264 near-inertial kinetic energy and vertical shear are only focused in anticyclonic regions with  
 265 Rossby number values of order  $0.1$ , rather than with those of order  $1$ . This suggests that  
 266 mesoscale anticyclones play a predominant role in determining the chimney effect.

267 Submesoscale processes are embedded in the field of mesoscale motions in the inner-  
 268 mooring diagnostics (Figures 3a and d). To isolate the submesoscale effect, we estimate

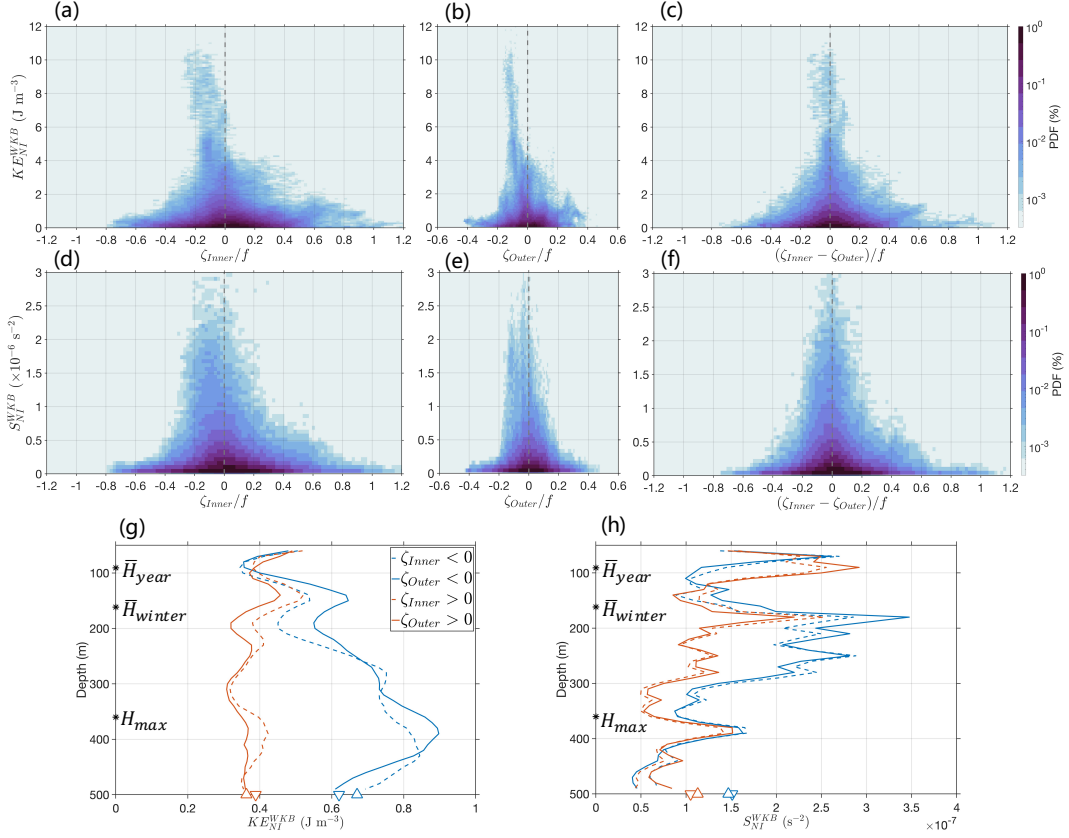


**Figure 3.** Two-dimensional probability density function of WKB-scaled near-inertial kinetic energy at the central mooring site,  $KE_{NI}^{WKB}$ , and Rossby number estimated from (a) the inner moorings,  $\zeta_{Inner}/f$ , (b) the outer moorings,  $\zeta_{Outer}/f$ , and (c) their difference,  $(\zeta_{Inner} - \zeta_{Outer})/f$ . (d-f) Same as (a-c) but for WKB-scaled near-inertial vertical shear,  $S_{NI}^{WKB}$ . Annual-averaged composite profiles of (g)  $KE_{NI}^{WKB}$  and (h)  $S_{NI}^{WKB}$  for positive and negative Rossby numbers. The annual-averaged, winter-averaged and maximum mixed layer depths, denoted by  $\bar{H}_{year}$ ,  $\bar{H}_{winter}$  and  $H_{max}$ , are marked on the y axis of (g-h). The upward-pointing and downward-pointing triangles on the x axis of (g-h) denote the averaged  $KE_{NI}^{WKB}$  and  $S_{NI}^{WKB}$  conditioned on the sign of vorticity from the outer and inner mooring clusters, respectively.

the submesoscale vorticity anomaly relative to the mesoscale background, that is,  $\zeta_{Inner} - \zeta_{Outer}$ . Figures 3c and f show that the association of enhanced  $KE_{NI}^{WKB}$  and  $S_{NI}^{WKB}$  with  $(\zeta_{Inner} - \zeta_{Outer})/f$  is greatly reduced, providing further evidence that the role played by submesoscale motions is modest and thus the observed chimney effect is attributed to mesoscale motions. Note, however, that submesoscale motions with spatial scales smaller than the inner mooring array are not resolved, and their role in modulating the chimney effect cannot be assessed. The detailed evolution of a near-inertial wave event with a mesoscale anticyclonic environment is provided in Figures S4-5, which illustrate the sequence from the wind forcing of mixed-layer inertial currents into NIWs shown as a set of discrete downward and rightward swaths below the mixed layer after approximately eight inertial periods. During the downward-propagating period, the mooring site was located inside an anticyclonic eddy with a Rossby number of order  $-0.1$ , as estimated from both the outer moorings and altimetric measurements.

We next examine the vertical structures of  $KE_{NI}^{WKB}$  and  $S_{NI}^{WKB}$  in regions of negative and positive vorticity (Figures 3g-h). The annual-averaged mixed layer depth is about 90 m. In the mixed layer, both  $KE_{NI}^{WKB}$  and  $S_{NI}^{WKB}$  show no clear dependence on relative vorticity. The muted chimney effect in the mixed layer is expected because wind-forced near-inertial oscillations are purely horizontal and thus are not influenced by the sign of relative vorticity (also see Figure 4). Below the base of the mixed layer, however,  $KE_{NI}^{WKB}$  associated with anticyclonic vorticity is substantially more energetic than that associated with cyclonic vorticity, typically by a factor of 2-3. This illustrates that near-inertial kinetic energy preferentially progresses downward in the presence of anticyclonic structures. In particular, the magnitude of  $KE_{NI}^{WKB}$  associated with anticyclonic vorticity gradually increases with depth and peaks at 400 m, consistent with an accumulation of trapped near-inertial kinetic energy at depth.

Compared to the cumulative behavior of  $KE_{NI}^{WKB}$  with depth,  $S_{NI}^{WKB}$  exhibits a different vertical structure. The peaks of  $S_{NI}^{WKB}$  associated with both cyclonic and anticyclonic vorticity are found around 180 m, which is very close to the mean mixed layer depth during winter (Figure 3h). Beneath 180 m,  $S_{NI}^{WKB}$  associated with cyclonic vorticity rapidly decreases from  $2.5 \times 10^{-7} \text{ s}^{-2}$  to about  $1 \times 10^{-7} \text{ s}^{-2}$ , and remains at this approximate magnitude down to 500 m. In contrast,  $S_{NI}^{WKB}$  associated with anticyclonic vorticity persists with an elevated magnitude of  $2.5 \times 10^{-7} \text{ s}^{-2}$  until an abrupt decrease occurs at approximately 300 m. Notably,  $S_{NI}^{WKB}$  in anticyclonic regions is always larger than that in cyclonic regions from 180 m down to approximately the deepest mixed layer depth of 360 m. Below 360 m,  $S_{NI}^{WKB}$ , again, shows no dependence on vorticity and gently decays with depth. These results suggest that high-mode NIWs, which are expected to dominate vertical shear, are likely dissipated near the base of the mixed layer, and only low-mode NIWs propagate further downward. We acknowledge, however, that accurate quantification of near-inertial kinetic energy distribution in barotropic and baroclinic modes from the moorings is particularly challenging, due to the limited sampling range (approximately one tenth of the full water column and one half of the water column above the mode-1 zero crossing; see Figure S6).

Apart from the background vorticity field, mesoscale straining processes may also affect the vertical propagation of NIWs (Bühler & McIntyre, 2005; Asselin et al., 2020; Noh & Nam, 2021). To further link the chimney effect to ambient flow properties, it can be instructive to apply the vorticity-strain parameter space (Balwada et al., 2021), which allows us to distinguish between strain-dominated regions (SD; i.e., fronts), anticyclonic vorticity-dominated regions (AVD; i.e., anticyclonic eddies) and cyclonic vorticity-dominated regions (CVD; i.e., cyclonic eddies). We examine the distributions of  $KE_{NI}^{WKB}$  and  $S_{NI}^{WKB}$  conditioned on the joint probability distribution function of outer mooring-based vorticity and strain within the mixed layer ( $|z| < H_{ML}$ ) and below the mixed layer ( $|z| > H_{ML}$ ) (Figures 4a-b). The strain rate is defined as  $\sigma = [(\frac{\partial u}{\partial x} - \frac{\partial v}{\partial y})^2 + (\frac{\partial u}{\partial y} + \frac{\partial v}{\partial x})^2]^{1/2}$ . The joint probability distribution functions below and within the mixed layer are qualitatively symmetric regarding vorticity, as expected at the mesoscales (Vic et al., 2022). Within the mixed layer,  $KE_{NI}^{WKB}$  and  $S_{NI}^{WKB}$  are homogeneously distributed in vorticity-strain space (Figures 4c and e). However, below the mixed layer, the largest values of  $KE_{NI}^{WKB}$  and  $S_{NI}^{WKB}$  are found in the AVD region (Figures 4d and f). This preference is also seen in the vertical structures of  $KE_{NI}^{WKB}$  and  $S_{NI}^{WKB}$  in regions of AVD, CVD and SD (Figures 4g and h), in particular for  $KE_{NI}^{WKB}$ . While the straining processes may have played a role in the conversion from inertial oscillations to NIWs, the deep penetration of NIWs is found to be mostly in anticyclonic eddies rather than strained regions. A similar pattern has been found through analysis of the inner moorings (Figure S7). This confirms that mesoscale anticyclonic eddies are the primary factor facilitating the deep penetration of surface-generated NIWs. The little influence of strain on NIWs conforms to expectations from the wave escape mechanism (Rocha et al., 2018), and was also reported in a dipole vortex in the Iceland Basin (Thomas et al., 2020).

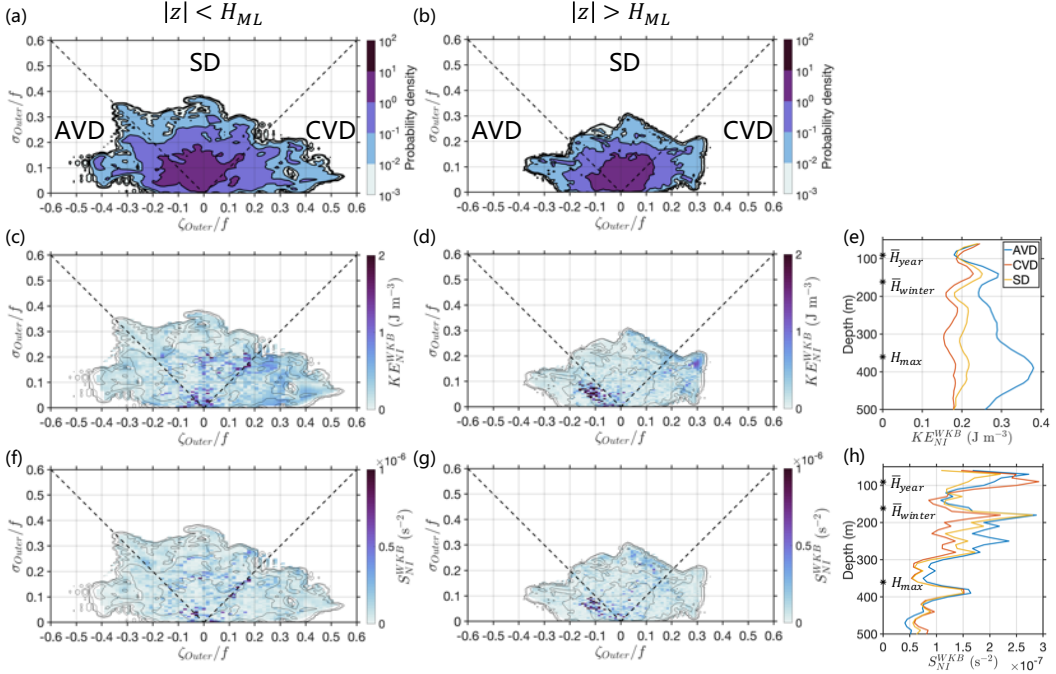


**Figure 4.** Vorticity-strain joint probability distribution function estimated from the outer moorings (a) within the mixed layer  $|z| < H_{ML}$  and (b) below the mixed layer  $|z| > H_{ML}$ . The x-y space is divided into three regions: anticyclonic vorticity dominated (AVD), cyclonic vorticity dominated (CVD), and strain dominated (SD). Conditional mean of (c-d)  $KE_{NI}^{WKB}$  and (f-g)  $S_{NI}^{WKB}$  conditioned on the vorticity and strain in the two vertical parts, contoured by the respective probability density. Annual-averaged composite profiles of (e)  $KE_{NI}^{WKB}$  and (h)  $S_{NI}^{WKB}$  for the AVD, CVD and SD regions. The annual-averaged, winter-averaged and maximum mixed layer depths, respectively denoted by  $\bar{H}_{year}$ ,  $\bar{H}_{winter}$  and  $H_{max}$ , are marked on the y axis of panels (e) and (h).

#### 4 Summary and Discussion

In this work, we have examined the annual cycle of NIWs in a typical open-ocean region at midlatitudes based on mooring observations. Our main findings are summarized as follows: (1) Local wind forcing is the main factor in generating near-inertial motions in the OSMOSIS region. Near-inertial kinetic energy is dominated by intermittent wind events of a few days duration, and shows a seasonal cycle in energy level, elevated in winter and reduced in summer. (2) Wind-generated NIWs are found to predominantly propagate equatorward and downward, with estimated horizontal group speeds two orders of magnitude larger than vertical group speeds. (3) The properties of NIWs have been estimated using the dispersion relation and observations, yielding an annual-mean frequency of  $1.039f$ , a vertical wavelength of 652 m and a horizontal wavelength of 79 km. We also demonstrate that the meridional group speed can be predicted from the vertical group speed diagnosed from a single mooring combined with the dispersion relation. (4) The penetration of near-inertial kinetic energy and vertical shear into the ocean interior is facilitated by mesoscale anticyclonic eddies with Rossby number of  $O(0.1)$  rather than submesoscale anticyclonic eddies with Rossby number of  $O(1)$ .

Our results add observational evidence for equatorward propagation of locally wind-generated NIWs, which conforms to expectations from the free propagation of NIWs due to  $\beta$ -refraction (Garrett, 2001). That is, waves generated at  $f$ , the local lowest internal

354 wave frequency, must propagate equatorward into a latitude with an inertial frequency  
 355 lower than  $f$ . The energy flux of these equatorward-propagating NIWs is dominated by low  
 356 modes (Alford, 2003), which are associated with a faster group velocity compared to high  
 357 modes and are typically expected to propagate over long distances.

358 The vertical structures of the chimney effect in mesoscale and submesoscale anticyclones  
 359 do not show a distinct difference (Figures 3g-h), suggesting that submesoscale processes  
 360 may not substantially modify the penetration of NIWs. There are three reasons for the  
 361 modest effect from the submesoscale. First, submesoscale motions are typically confined  
 362 to the mixed layer of  $O(100\text{ m})$  and weaken in the ocean interior. Mixed-layer inertial  
 363 oscillations may undergo lateral de-phasing caused by submesoscale motions, which would  
 364 produce downward-propagating NIWs with small vertical scales, and thus the resulting  
 365 vertical group velocity would be small. By contrast, mesoscale eddies are featured with a  
 366 much larger vertical scale on the order of  $1000\text{ m}$ , and thus can be a primary player in  
 367 setting the inertial chimney effect at depth. Second, the spatial scale of submesoscales is  
 368 comparable to the local mixed-layer Rossby radius of  $1\text{-}4\text{ km}$  (Yu et al., 2019; Callies et  
 369 al., 2020), which is considerably smaller than the diagnosed spatial scale of NIWs ( $2\pi/k_h =$   
 370  $79\text{ km}$ ). Third, both NIWs and submesoscale fronts are intermittent and short-lived in the  
 371 study region, and thus the concurrence of both processes is even rarer.

372 Lastly, this study points out the importance of the inertial chimney effect in deter-  
 373 mining surface-generated near-inertial kinetic energy propagation into the ocean interior.  
 374 However, the interactions of NIWs with eddies and associated energy transfers are not a  
 375 direct consequence of the chimney effect. It has recently been suggested that the presence  
 376 of NIWs can result in a substantial reduction of mesoscale kinetic energy by stimulating  
 377 a forward energy cascade at partially-balanced submesoscale fronts (Barkan et al., 2021).  
 378 The assessment and quantification of such cross-scale energy transfers using the OSMOSIS  
 379 observations are under way.

### 380 Acknowledgments

381 We are grateful to the officers, crew, scientists and technicians of the RRS *Discovery*,  
 382 RRS *James Cook*, and R/V *Celtic Explorer*, for their hard work in deploying and recov-  
 383 ering the OSMOSIS moorings and gliders. All data are archived at the British Oceanog-  
 384 graphic Data Centre (glider data are accessible at <https://doi.org/10/cqc6>). This work was  
 385 funded by grants from the Natural Environmental Research Council (NE/I019999/1 and  
 386 NE/I01993X/1). ERA-Interim data were obtained from the European Centre for Medium-  
 387 Range Weather Forecasts (downloaded from <http://www.ecmwf.int/en/research/climate->  
 388 [reanalysis/era-interim](#)).

389 **References**

- 390 Alford, M. H. (2003). Redistribution of energy available for ocean mixing by long-range  
391 propagation of internal waves. *Nature*, 423(6936), 159-162.
- 392 Alford, M. H. (2020). Revisiting near-inertial wind work: Slab models, relative stress, and  
393 mixed layer deepening. *Journal of Physical Oceanography*, 50(11), 3141–3156.
- 394 Alford, M. H., MacKinnon, J. A., Pinkel, R., & Klymak, J. M. (2017). Space-time scales  
395 of shear in the North Pacific. *Journal of Physical Oceanography*, 47(10), 2455–2478.
- 396 Alford, M. H., MacKinnon, J. A., Simmons, H. L., & Nash, J. D. (2016). Near-inertial  
397 internal gravity waves in the ocean. *Annual Review of Marine Science*, 8, 95-123.
- 398 Alford, M. H., & Zhao, Z. X. (2007). Global patterns of low-mode internal-wave propagation.  
399 part i: Energy and energy flux. *Journal of Physical Oceanography*, 37(7), 1829-1848.
- 400 Asselin, O., Thomas, L. N., Young, W. R., & Rainville, L. (2020). Refraction and straining  
401 of near-inertial waves by barotropic eddies. *Journal of Physical Oceanography*, 50(12),  
402 3439–3454.
- 403 Asselin, O., & Young, W. R. (2020). Penetration of wind-generated near-inertial waves into  
404 a turbulent ocean. *Journal of Physical Oceanography*, 50(6), 1699–1716.
- 405 Balwada, D., Xiao, Q., Smith, S., Abernathey, R., & Gray, A. R. (2021). Vertical fluxes  
406 conditioned on vorticity and strain reveal submesoscale ventilation. *Journal of Physical  
407 Oceanography*, 51(9), 2883–2901.
- 408 Barkan, R., Srinivasan, K., Yang, L., McWilliams, J. C., Gula, J., & Vic, C. (2021). Oceanic  
409 mesoscale eddy depletion catalyzed by internal waves. *Geophysical Research Letters*,  
410 48(18).
- 411 Buckingham, C. E., Garabato, A. C. N., Thompson, A. F., Brannigan, L., Lazar, A., Mar-  
412 shall, D. P., ... Belcher, S. E. (2016). Seasonality of submesoscale flows in the ocean  
413 surface boundary layer. *Geophysical Research Letters*, 43(5), 2118-2126.
- 414 Buckingham, C. E., Lucas, N. S., Belcher, S. E., Rippeth, T. P., Grant, A. L. M., Le Sommer,  
415 J., ... Naveira Garabato, A. C. (2019). The contribution of surface and submesoscale  
416 processes to turbulence in the open ocean surface boundary layer. *Journal of Advances  
417 in Modeling Earth Systems*, 11(12), 4066–4094.
- 418 Bühler, O., & McIntyre, M. E. (2005). Wave capture and wave-vortex duality. *Journal of  
419 Fluid Mechanics*, 534, 67–95.
- 420 Callies, J., Barkan, R., & Naveira Garabato, A. C. (2020). Time scales of submesoscale flow  
421 inferred from a mooring array. *Journal of Physical Oceanography*, 50(4), 1065–1086.
- 422 Chaigneau, A., Pizarro, O., & Rojas, W. (2008). Global climatology of near-inertial current  
423 characteristics from lagrangian observations. *Geophysical Research Letters*, 35(13).
- 424 Damerell, G. M., Heywood, K. J., Thompson, A. F., Binetti, U., & Kaiser, J. (2016). The  
425 vertical structure of upper ocean variability at the porcupine abyssal plain during  
426 2012-2013. *Journal of Geophysical Research-Oceans*, 121(5), 3075-3089.
- 427 Dee, D. P., Uppala, S. M., Simmons, A. J., Berrisford, P., Poli, P., Kobayashi, S., ... Vitart,  
428 F. (2011). The era-interim reanalysis: configuration and performance of the data  
429 assimilation system. *Quarterly Journal of the Royal Meteorological Society*, 137(656),  
430 553-597.
- 431 Egbert, G. D., & Ray, R. D. (2000). Significant dissipation of tidal energy in the deep ocean  
432 inferred from satellite altimeter data. *Nature*, 405, 775–778.
- 433 Erickson, Z. K., Thompson, A. F., Callies, J., Yu, X. L., Garabato, A. N., & Klein, P.  
434 (2020). The vertical structure of open-ocean submesoscale variability during a full  
435 seasonal cycle. *Journal of Physical Oceanography*, 50(1), 145-160.
- 436 Ferrari, R., & Wunsch, C. (2009). Ocean circulation kinetic energy: Reservoirs, sources,  
437 and sinks. *Annual Review of Fluid Mechanics*, 41, 253-282.
- 438 Fu, L. L. (1981). Observations and models of inertial waves in the deep ocean. *Reviews of  
439 Geophysics*, 19(1), 141-170.
- 440 Garrett, C. (2001). What is the "near-inertial" band and why is it different from the rest  
441 of the internal wave spectrum? *Journal of Physical Oceanography*, 31(4), 962-971.
- 442 Gill, A. E. (1984). On the behavior of internal waves in the wakes of storms. *Journal of  
443 Physical Oceanography*, 14(7), 1129-1151.

- Huang, R., Xie, X., Hu, J., & Sun, Z. (2021). Poleward propagation of typhoon-induced near-inertial waves in the northern south china sea. *Frontiers in Marine Science*, 8, 713991.
- Jeon, C., Park, J.-H., Nakamura, H., Nishina, A., Zhu, X.-H., Kim, D. G., ... Hirose, N. (2019). Poleward-propagating near-inertial waves enabled by the western boundary current. *Scientific Reports*, 9(1), 9955.
- Jiang, J., Lu, Y. Y., & Perrie, W. (2005). Estimating the energy flux from the wind to ocean inertial motions: The sensitivity to surface wind fields. *Geophysical Research Letters*, 32(15).
- Kunze, E. (1985). Near-inertial wave-propagation in geostrophic shear. *Journal of Physical Oceanography*, 15(5), 544-565.
- Large, W. G., & Pond, S. (1981). Open ocean momentum flux measurements in moderate to strong winds. *Journal of Physical Oceanography*, 11(3), 324-336.
- Leaman, K. D., & Sanford, T. B. (1975). Vertical energy propagation of inertial waves - vector spectral analysis of velocity profiles. *Journal of Geophysical Research*, 80(15), 1975-1978.
- Lee, D.-K., & Niiler, P. P. (1998). The inertial chimney: The near-inertial energy drainage from the ocean surface to the deep layer. *Journal of Geophysical Research: Oceans*, 103(C4), 7579-7591.
- Naveira Garabato, A. C., Yu, X., Callies, J., Barkan, R., Polzin, K. L., Frajka-Williams, E., ... Griffies, S. M. (2022). Kinetic energy transfers between mesoscale and submesoscale motions in the open ocean's upper layers. *Journal of Physical Oceanography*, 52(1), 75-97.
- Noh, S., & Nam, S. (2021). Nonseasonal variations in near-inertial kinetic energy observed far below the surface mixed layer in the southwestern east sea (Japan Sea). *Journal of Marine Science and Engineering*, 10(1), 9.
- Park, J. J., Kim, K., & King, B. A. (2005). Global statistics of inertial motions. *Geophysical Research Letters*, 32(14).
- Plueddemann, A. J., & Farrar, J. T. (2006). Observations and models of the energy flux from the wind to mixed-layer inertial currents. *Deep-Sea Research Part II-Topical Studies in Oceanography*, 53(1-2), 5-30.
- Qu, L., Thomas, L., & Gula, J. (2021). Bottom mixing enhanced by tropical storm-generated near-inertial waves entering critical layers in the Straits of Florida. *Geophysical Research Letters*, 48(15), e2021GL093773.
- Raja, K. J., Buijsman, M. C., Shriver, J. F., Arbic, B. K., & Siyanbola, O. (2022). Near-inertial wave energetics modulated by background flows in a global model simulation. *Journal of Physical Oceanography*, in press. doi: 10.1175/JPO-D-21-0130.1
- Rimac, A., von Storch, J. S., Eden, C., & Haak, H. (2013). The influence of high-resolution wind stress field on the power input to near-inertial motions in the ocean. *Geophysical Research Letters*, 40(18), 4882-4886.
- Rocha, C. B., Wagner, G. L., & Young, W. R. (2018). Stimulated generation: extraction of energy from balanced flow by near-inertial waves. *Journal of Fluid Mechanics*, 847, 417-451.
- Schlosser, T. L., Jones, N. L., Bluteau, C. E., Alford, M. H., Ivey, G. N., & Lucas, A. J. (2019). Generation and propagation of near-inertial waves in a baroclinic current on the Tasmanian Shelf. *Journal of Physical Oceanography*, 49(10), 2653-2667.
- Silverthorne, K. E., & Toole, J. M. (2009). Seasonal kinetic energy variability of near-inertial motions. *Journal of Physical Oceanography*, 39(4), 1035-1049.
- Simmons, H. L., & Alford, M. H. (2012). Simulating the long-range swell of internal waves generated by ocean storms. *Oceanography*, 25(2), 30-41.
- Thomas, L. N., Rainville, L., Asselin, O., Young, W. R., Girton, J., Whalen, C. B., ... Hormann, V. (2020). Direct observations of near-inertial wave  $\zeta$ -refraction in a dipole vortex. *Geophysical Research Letters*, 47(21).
- Thomas, L. N., & Zhai, X. (2022). *Chapter 5 - the lifecycle of surface-generated near-inertial waves* (M. Meredith & A. Naveira Garabato, Eds.). Elsevier.

- 499 Thompson, A. F., Lazar, A., Buckingham, C., Garabato, A. C. N., Damerell, G. M., &  
500 Heywood, K. J. (2016). Open-ocean submesoscale motions: A full seasonal cycle  
501 of mixed layer instabilities from gliders. *Journal of Physical Oceanography*, 46(4),  
502 1285–1307.
- 503 Tort, M., & Winters, K. B. (2018). Poleward propagation of near-inertial waves induced by  
504 fluctuating winds over a baroclinically unstable zonal jet. *Journal of Fluid Mechanics*,  
505 834, 510–530.
- 506 Vic, C., Ferron, B., Thierry, V., Mercier, H., & Lherminier, P. (2021). Tidal and near-  
507 inertial internal waves over the Reykjanes Ridge. *Journal of Physical Oceanography*,  
508 51(2), 419–437.
- 509 Vic, C., Hascoët, S., Gula, J., Huck, T., & Maes, C. (2022). Oceanic mesoscale cyclones  
510 cluster surface lagrangian material. *Geophysical Research Letters*, 49(4).
- 511 Whalen, C. B., de Lavergne, C., Naveira Garabato, A. C., Klymak, J. M., MacKinnon,  
512 J. A., & Sheen, K. L. (2020). Internal wave-driven mixing: governing processes and  
513 consequences for climate. *Nature Reviews Earth & Environment*, 1(11), 606–621.
- 514 Yu, X., Naveira Garabato, A. C., Martin, A. P., Buckingham, C. E., Brannigan, L., & Su,  
515 Z. (2019). An annual cycle of submesoscale vertical flow and restratification in the  
516 upper ocean. *Journal of Physical Oceanography*, 49(6), 1439–1461.
- 517 Yu, X., Naveira Garabato, A. C., Martin, A. P., & Marshall, D. P. (2021). The annual cycle  
518 of upper-ocean potential vorticity and its relationship to submesoscale instabilities.  
519 *Journal of Physical Oceanography*, 51(2), 385–402.
- 520 Zhai, X. M., Greatbatch, R. J., & Eden, C. (2007). Spreading of near-inertial energy in  
521 a  $1/12^\circ$  model of the North Atlantic Ocean. *Geophysical Research Letters*, 34(10),  
522 L10609.
- 523 Zhai, X. M., Greatbatch, R. J., Eden, C., & Hibiya, T. (2009). On the loss of wind-induced  
524 near-inertial energy to turbulent mixing in the upper ocean. *Journal of Physical  
525 Oceanography*, 39(11), 3040–3045.
- 526 Zhai, X. M., Greatbatch, R. J., & Zhao, J. (2005). Enhanced vertical propagation of storm-  
527 induced near-inertial energy in an eddying ocean channel model. *Geophysical Research  
528 Letters*, 32(18).

# Supporting Information for “Observed equatorward propagation and chimney effect of near-inertial waves in the mid-latitude ocean”

Xiaolong Yu<sup>1,2,3</sup>, Alberto C. Naveira Garabato<sup>4</sup>, Clément Vic<sup>5</sup>, Jonathan

Gula<sup>5,6</sup>, Anna C. Savage<sup>7</sup>, Jinbo Wang<sup>8</sup>, Amy F. Waterhouse<sup>7</sup>, Jennifer A.

MacKinnon<sup>7</sup>

<sup>1</sup>School of Marine Sciences, Sun Yat-sen University, Zhuhai, China

<sup>2</sup>Southern Marine Science and Engineering Guangdong Laboratory (Zhuhai), Zhuhai, China

<sup>3</sup>Guangdong Provincial Key Laboratory of Marine Resources and Coastal Engineering, Guangzhou, China

<sup>4</sup>Ocean and Earth Science, University of Southampton, Southampton, UK

<sup>5</sup>Univ Brest, CNRS, IRD, Ifremer, Laboratoire d’Océanographie Physique et Spatiale (LOPS), IUEM, Brest, France

<sup>6</sup>Institut Universitaire de France (IUF), Paris, France

<sup>7</sup>Scripps Institution of Oceanography, University of California, San Diego, La Jolla, California, USA

<sup>8</sup>Jet Propulsion Laboratory, California Institute of Technology, Pasadena, California, USA

## Contents of this file

1. Text S1 to S3
2. Table S1
3. Figures S1 to S7

### Text S1. Wentzel-Kramers-Brillouin scaling

The amplitude and wavenumber of NIWs change with the varying vertical stratification in the ocean due to refraction (Leaman & Sanford, 1975). To account for this effect, ‘Wentzel-Kramers-Brillouin (WKB) scale’ and ‘WKB stretch’ are typically applied (e.g., Bell, 1974; Duda & Cox, 1989). As previous OSMOSIS studies have shown that the region underwent a seasonal cycle on the vertical stratification (e.g., Buckingham et al., 2016; Erickson et al., 2020), monthly moving averaged buoyancy frequency is used to get WKB scaling from the time series of horizontal velocity. The WKB-scaled (denoted by the superscript ‘*WKB*’) near-inertial kinetic energy is computed as

$$KE_{NI}^{WKB} = \frac{\bar{N}(t)}{N(t, z)} KE_{NI}, \quad (1)$$

where  $t$  is the time,  $z$  is the vertical coordinate,  $N = \sqrt{-(g/\rho_0)(\partial\rho/\partial z)}$  is the buoyancy frequency with  $g$  as gravity and  $\rho$  as potential density, and  $\bar{N}$  denotes the depth-mean buoyancy frequency between 50 and 520 m. Similarly, the WKB-scaled near-inertial vertical shear is computed as

$$S_{NI}^{WKB} = \frac{\bar{N}(t)}{N(t, z)} |\partial\mathbf{u}_{NI}/\partial z|^2. \quad (2)$$

To account for vertical wavenumber changes, the WKB-stretched depth is computed as

$$z^{WKB} = \int_{-50}^z \frac{N(z)}{\bar{N}} dz, \quad (3)$$

where  $z^{WKB}$  is the stretched vertical coordinate. Quantitative calculations such as the seasonal rotary vertical wavenumber spectrum are computed in the stretched coordinates (Figure S3).

## Text S2. Slab model

Slab models have been found appropriate for reproducing near-inertial motions in the mixed layer from time series of wind alone (e.g., Pollard & Millard, 1970; Plueddemann & Farrar, 2006). The corresponding momentum equation can be expressed as

$$\frac{d\tilde{\mathbf{u}}}{dt} + (r + if)\tilde{\mathbf{u}} = \frac{\tilde{\boldsymbol{\tau}}}{\rho_0 H_{ML}}, \quad (4)$$

where  $(\tilde{\cdot})$  denotes the complex format (e.g.,  $\tilde{\mathbf{u}} = u + iv$ ),  $r$  is a damping constant that parameterizes the transfer of energy from the mixed layer to the ocean interior and  $H_{ML}$  is the mixed layer depth. Here we use a damping factor  $r = 0.04f$  ( $r^{-1} \sim 16.7$  days), consistent with previous work (e.g., D'Asaro, 1985; Alford et al., 2012). The 10-day smoothed mixed layer depth estimated from the OSMOSIS gliders is used. The slab model is solved using the traditional time-stepping method (D'Asaro, 1985).

## Text S3. Dispersion relation and near-inertial properties

Following Gill (1982), the dispersion relation for NIWs in the absence of background flows is given by

$$(\omega^2 - f^2)m^2 = N^2 k_h^2, \quad (5)$$

where  $\omega$  is the frequency,  $m$  the vertical wavenumber and  $k_h$  the horizontal wavenumber. The vertical group speed  $c_{gz}$  can then be derived by taking the derivative of the dispersion relation with respect to vertical wavenumber, yielding

$$c_{gz} = \frac{\partial \omega}{\partial m} = (\omega^2 - f^2)/\omega m. \quad (6)$$

Similarly, the horizontal group speed  $c_{gh}$  can be estimated by

$$c_{gh} = \frac{\partial \omega}{\partial k_h} = N \sqrt{\omega^2 - f^2}/\omega m. \quad (7)$$

Thus, a relationship between  $c_{gz}$  and  $c_{gh}$  can be obtained as follows:

$$\frac{c_{gz}}{c_{gh}} = \sqrt{\omega^2 - f^2}/N. \quad (8)$$

From equation (8) and mooring-inferred horizontal and vertical group speeds, the equation for  $\omega$  is

$$\omega = \sqrt{f^2 + N^2 \frac{(c_{gz}^{obs})^2}{(c_{gh}^{obs})^2}}. \quad (9)$$

Then the horizontal wavenumber can be obtained by

$$k_h = \sqrt{\frac{(\omega^2 - f^2)m^2}{N^2}}. \quad (10)$$

The buoyancy frequency  $N = 3.5 \times 10^{-3}$  rad s<sup>-1</sup> ( $N/f \sim 31$ ) is computed from climatological temperature and salinity profiles of the World Ocean Atlas 2018 (Garcia et al., 2019), and then averaged over the 50–520-m depth range.

## References

- Alford, M. H., Cronin, M. F., & Klymak, J. M. (2012). Annual cycle and depth penetration of wind-generated near-inertial internal waves at ocean station papa in the northeast pacific. *Journal of Physical Oceanography*, 42(6), 889-909.
- Bell, T. H. (1974). Processing vertical internal wave spectra. *Journal of Physical Oceanography*, 4, 669–670.
- Buckingham, C. E., Garabato, A. C. N., Thompson, A. F., Brannigan, L., Lazar, A., Marshall, D. P., ... Belcher, S. E. (2016). Seasonality of submesoscale flows in the ocean surface boundary layer. *Geophysical Research Letters*, 43(5), 2118-2126.
- D'Asaro, E. A. (1985). The energy flux from the wind to near-inertial motions in the surface mixed layer. *Journal of Physical Oceanography*, 15(8), 1043-1059.

- Duda, T. F., & Cox, C. S. (1989). Vertical wave number spectra of velocity and shear at small internal wave scales. *Journal of Geophysical Research*, 94(C1), 939.
- Erickson, Z. K., Thompson, A. F., Callies, J., Yu, X. L., Garabato, A. N., & Klein, P. (2020). The vertical structure of open-ocean submesoscale variability during a full seasonal cycle. *Journal of Physical Oceanography*, 50(1), 145-160.
- Garcia, H. E., Boyer, T. P., Baranova, O. K., Locarnini, R. A., Mishonov, A. V., Grodsky, A., ... Zweng, M. M. (2019). *World Ocean Atlas 2018: Product documentation* (A. Mishonov, Ed.).
- Gill, A. E. (1982). *Atmosphere-ocean dynamics*. Academic Press New York.
- Leaman, K. D., & Sanford, T. B. (1975). Vertical energy propagation of inertial waves - vector spectral analysis of velocity profiles. *Journal of Geophysical Research*, 80(15), 1975-1978.
- Plueddemann, A. J., & Farrar, J. T. (2006). Observations and models of the energy flux from the wind to mixed-layer inertial currents. *Deep-Sea Research Part II-Topical Studies in Oceanography*, 53(1-2), 5-30.
- Pollard, R. T., & Millard, R. C. (1970). Comparison between observed and simulated wind-generated inertial oscillations. *Deep-Sea Research*, 17(4), 813-821.

**Table S1.** Detailed properties of the six near-inertial events derived from the mooring observations combined with the dispersion relation.

| Event    | $c_{gz}^{obs}$ [m d $^{-1}$ ] | $c_{gh}^{obs}$ [m day $^{-1}$ ] | $\omega$           | $2\pi/m$ [m] | $2\pi/k_h$ [km] |
|----------|-------------------------------|---------------------------------|--------------------|--------------|-----------------|
| 1        | 79                            | 5875                            | $1.065f$           | 781          | 69              |
| 2        | 59                            | 6653                            | $1.036f$           | 787          | 94              |
| 3        | 50                            | 5270                            | $1.026f$           | 342          | 48              |
| 4        | 75                            | 4838                            | $1.058f$           | 513          | 48              |
| 5        | 47                            | 7085                            | $1.023f$           | 791          | 119             |
| 6        | 58                            | 5270                            | $1.029f$           | 698          | 93              |
| mean±std | 61±13                         | 5875±864                        | $1.039 \pm 0.018f$ | 652±185      | 79±28           |

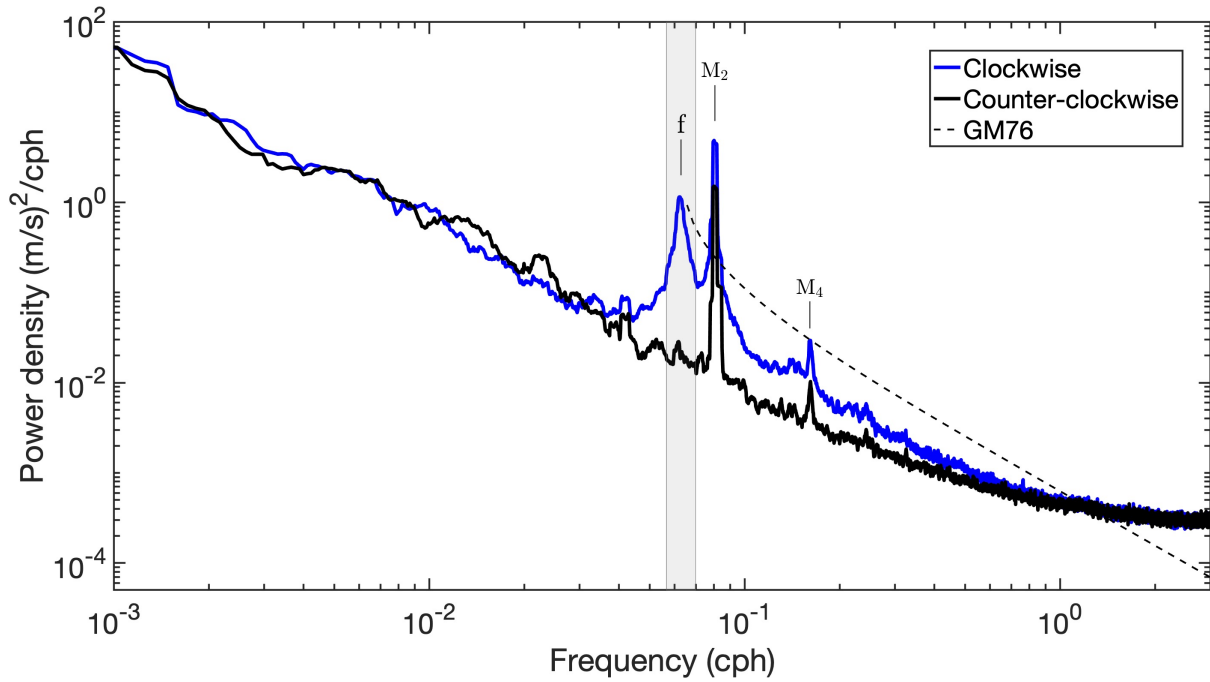


**Figure S1.** Rotary frequency spectrum of WKB-scaled horizontal velocity measured by the top current meter on the central mooring with the record period September 2012 – September 2013. The clockwise and counter-clockwise components of the spectrum are blue and black, respectively. The GM76 model spectrum is indicated by a black dashed curve. The inertial peak (1/15.91 cph), M2 (1/12.42 cph) and M4 (1/6.21 cph) tidal peaks are marked. The light grey shaded region indicates the near-inertial band used in band-pass filter to isolate near-inertial signals.

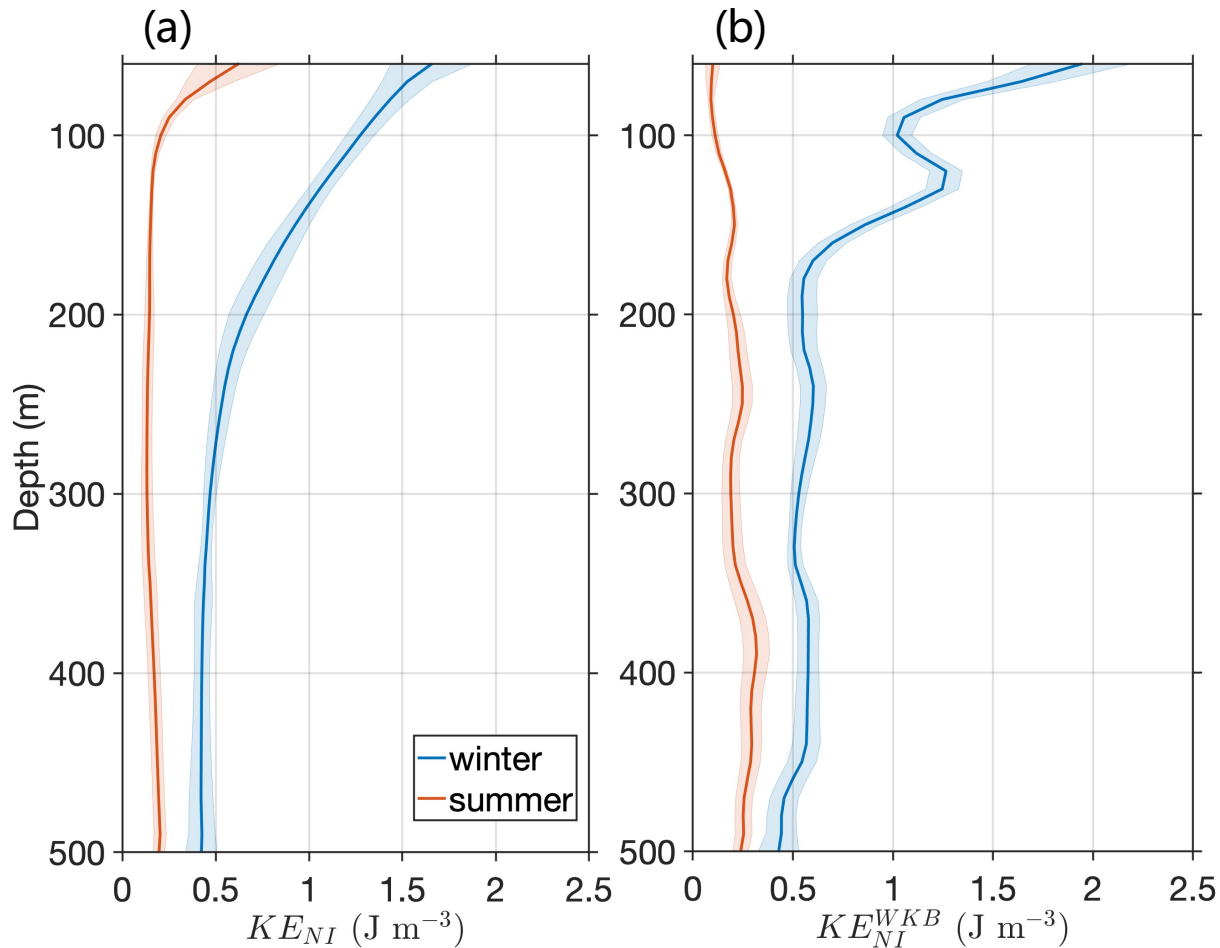


**Figure S2.** The time-mean profiles (solid lines) and one standard deviation envelope respective to all nine moorings (shading) of (a) measured and (b) WKB-scaled near-inertial kinetic energy in winter (December–February; blue) and summer (June–August; orange).

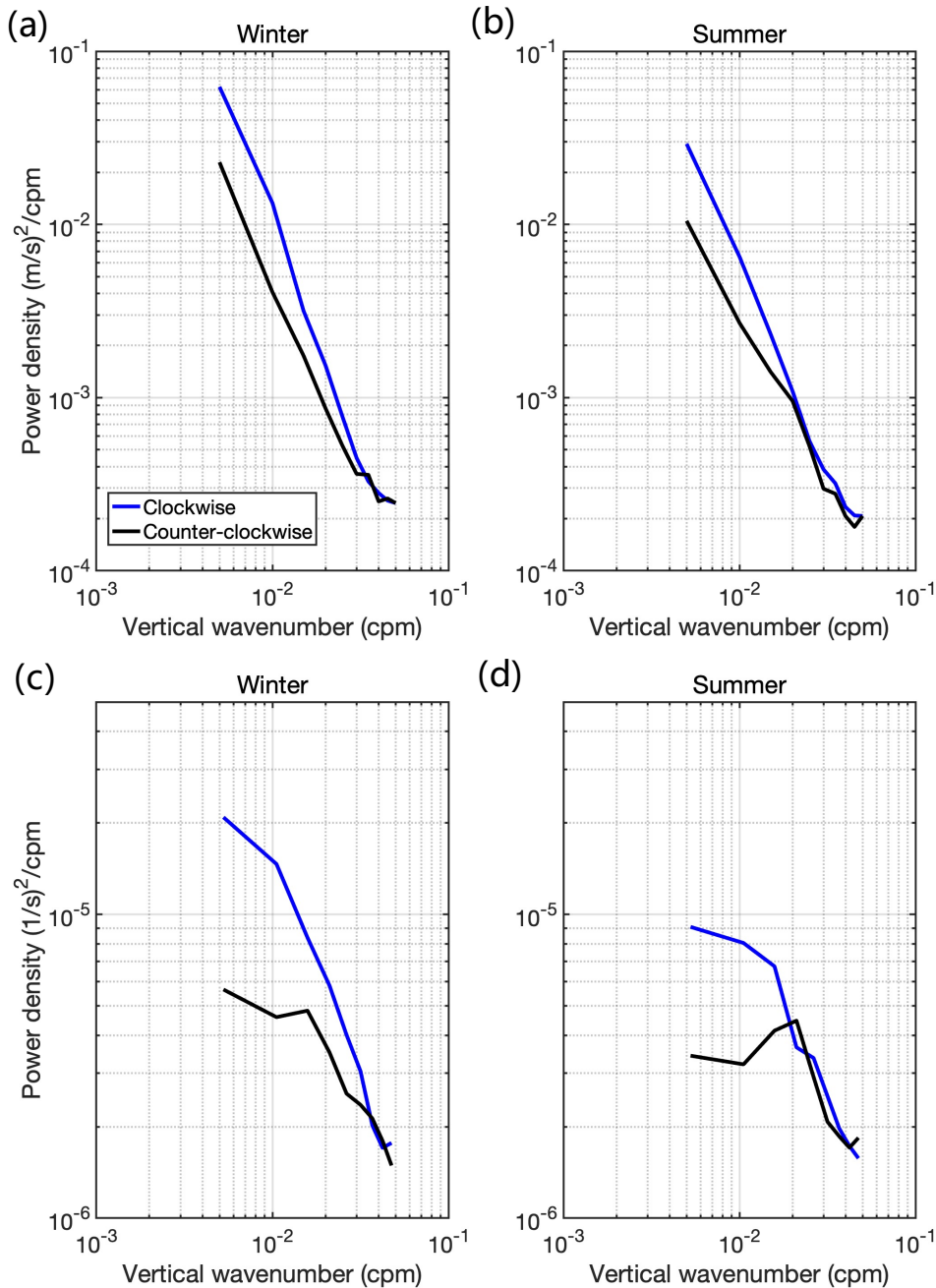


**Figure S3.** Rotary vertical wavenumber spectra of the WKB-scaled near-inertial velocity profiles (top) and the WKB-scaled near-inertial vertical shear profiles (bottom) from the ADCP measurements, showing the clockwise (blue) and the counter-clockwise (black) components. The (left) wintertime and (right) summertime horizontal velocity spectra are calculated as the mean of respective period.

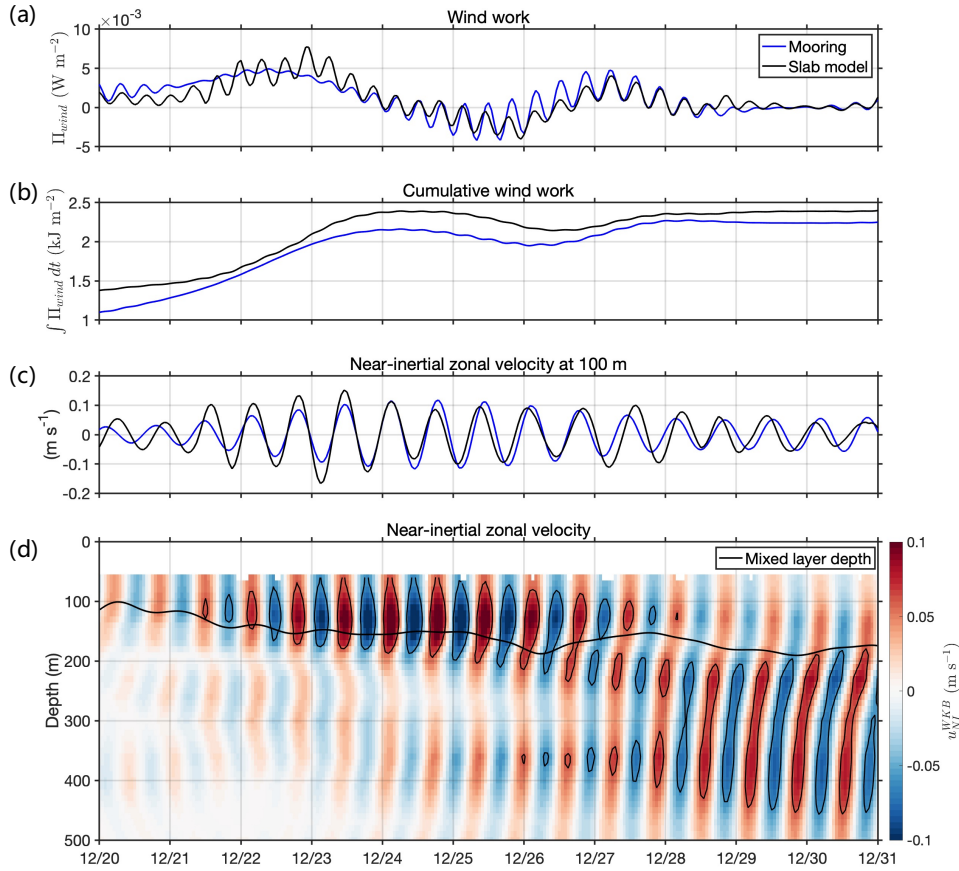


**Figure S4.** Observed and modeled wind work and upper-ocean currents during a near-inertial wave event (20 - 31 December 2012). (a) Energy flux into near-inertial motions from observed mixed-layer near-inertial currents and reanalysis winds (blue line) and slab model driven by reanalysis winds (black line). (b) The time integral of (a) showing the cumulative energy input to the mixed layer from each flux estimate. (c) Zonal mixed-layer near-inertial current from the top ACM sensor (blue), and zonal mixed-layer current estimated from the slab model driven by reanalysis winds (black). (d) Near-inertial zonal velocity from the ACMs. Black contours mark the velocity of  $0.1 \text{ m s}^{-1}$ . The black line represents the glider-derived mixed layer depth.

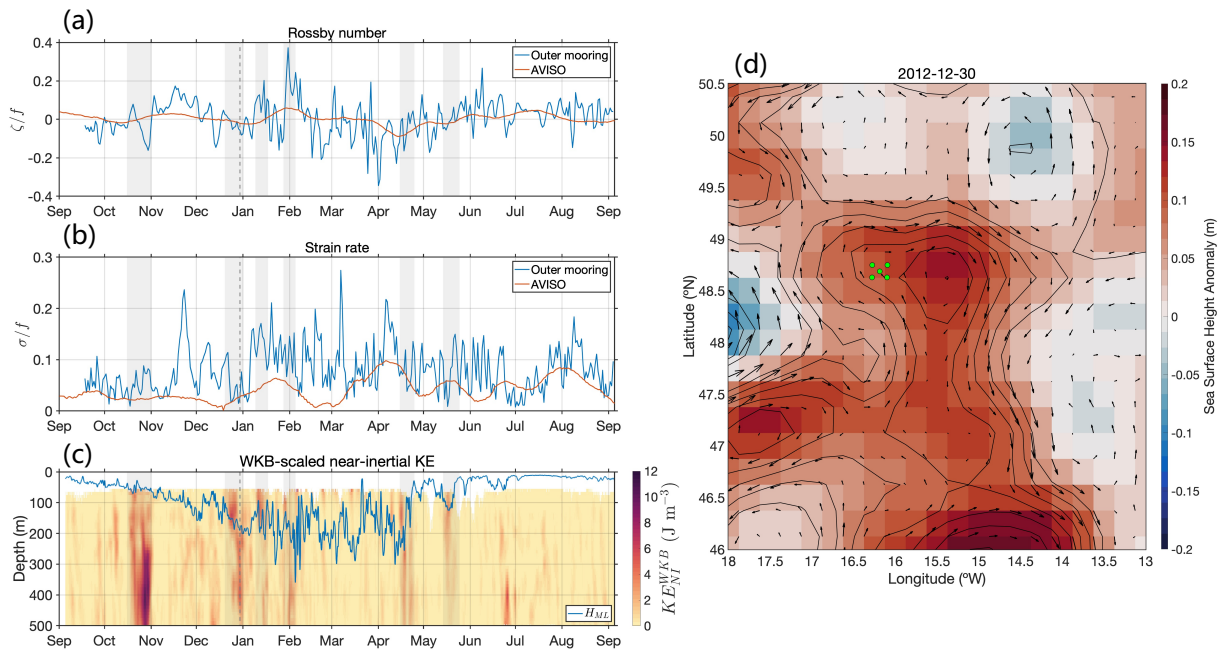


**Figure S5.** (a) Time series of Rossby number estimated from the outer moorings (depth-averaged; blue) and altimetric measurements (orange). (b) Time series of strain rate estimated from the outer moorings (depth-averaged; blue) and altimetric measurements (orange). (c) WKB-scaled near-inertial kinetic energy observed from the current meters at the central mooring. The blue line indicates the glider-based mixed layer depth  $H_{ML}$ . Grey shaded regions in (a-c) indicate the six wind-generated events of NIWs. (d) Snapshot of sea level anomaly on 30 December 2012 with surface geostrophic current velocity shown as black vectors and the sea level anomaly contours (0.04-m interval, ranging from -0.2 to 0.2 m). Sea level anomaly and surface geostrophic velocity data are obtained from the delayed-time gridded  $0.25^\circ \times 0.25^\circ$  AVISO (Archiving, Validation and Interpretation of Satellite Oceanographic Data) product. The green dots indicate the location of the OSMOSIS central and outer moorings. The grey dashed lines in (a-c) indicate the time of 30 December 2012.

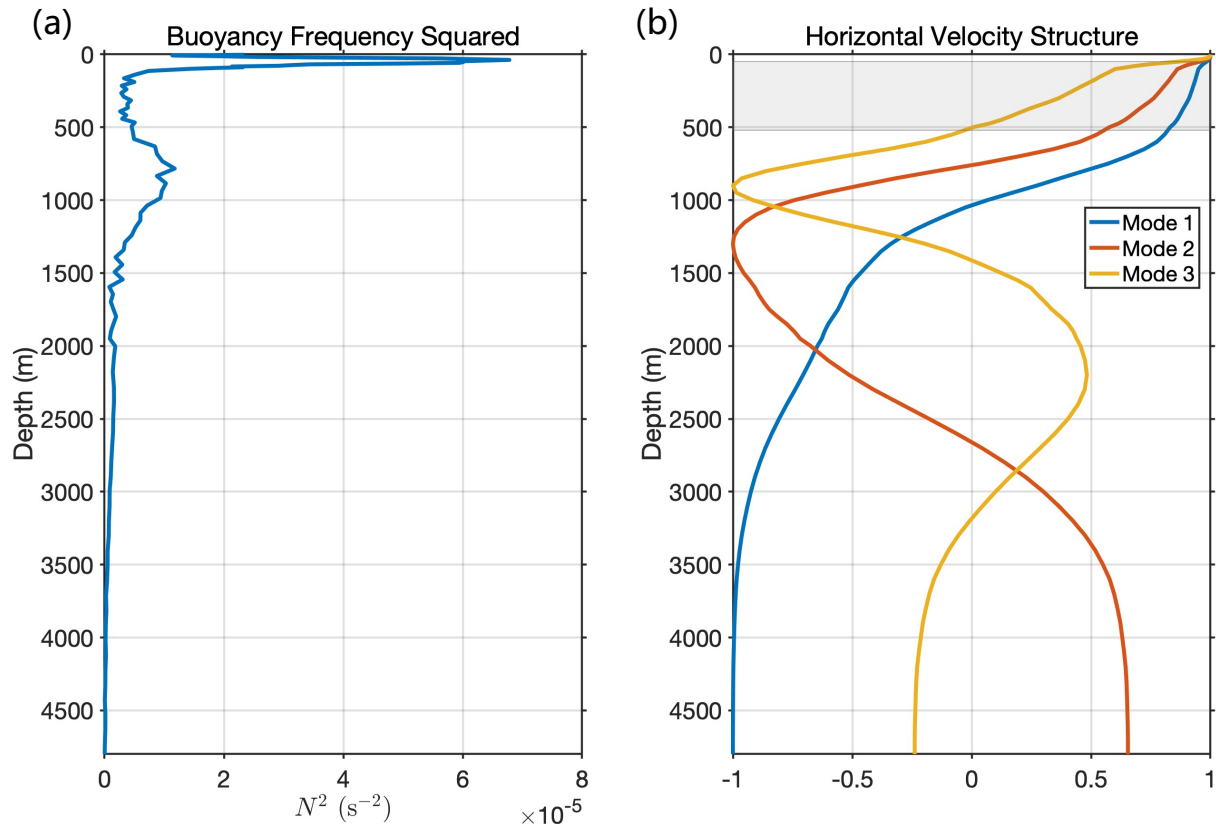


**Figure S6.** (a) Climatological mean stratification  $N^2$  computed from WOA18 at the point nearest to the mooring site and (b) the first three modes for horizontal velocity. Grey shading represent the central mooring's vertical sampling range.

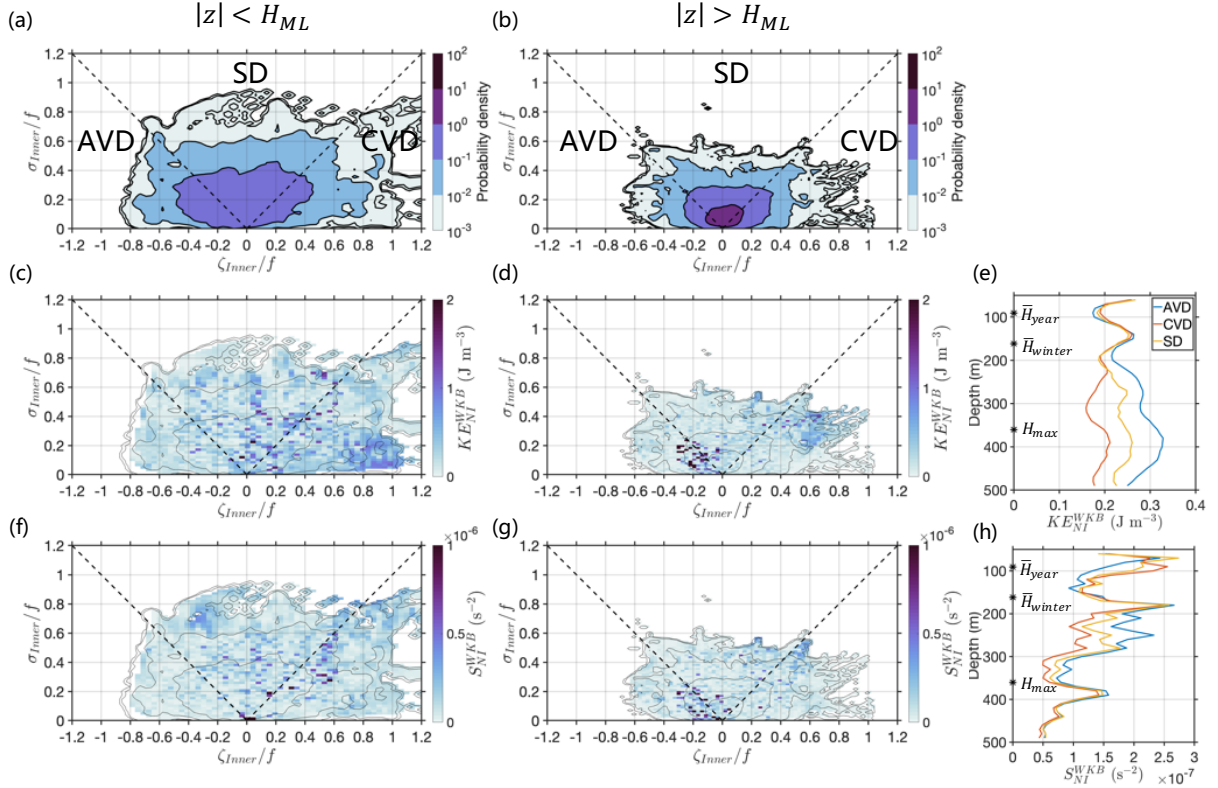


**Figure S7.** Vorticity-strain joint probability density function estimated from the inner moorings (a) within the mixed layer  $|z| < H_{ML}$  and (b) below the mixed layer  $|z| > H_{ML}$ . The x-y space is divided into three regions: anticyclonic vorticity dominated (AVD), cyclonic vorticity dominated (CVD), and strain dominated (SD). Conditional mean of (c-d)  $KE_{NI}^{WKB}$  and (f-g)  $S_{NI}^{WKB}$  conditioned on the vorticity and strain in the two vertical parts, contoured by the respective probability density. Annual-averaged composite profiles of (e)  $KE_{NI}^{WKB}$  and (h)  $S_{NI}^{WKB}$  for the AVD, CVD and SD regions. The annual-averaged, winter-averaged and maximum mixed layer depths, respectively denoted by  $\bar{H}_{year}$ ,  $\bar{H}_{winter}$  and  $H_{max}$ , are marked on the y axis of panels (e) and (h).